Supplement of: Decadal transition of $PM_{2.5}$ source structure over North China: Weakening combustion and emerging nitrate-driven pollution

This supplement provides detailed information on chemical analysis, quality control, and sample grouping, PMF model diagnostics, sensitivity tests for the high-$PM_{2.5}$ threshold, seasonal sensitivity, and ISORROPIA-II thermodynamic diagnostics. The main findings are presented in the manuscript; this document retains only the necessary methodological notes, complete data tables, and robustness checks.

Contents

Text S1. Detailed chemical analysis, quality control, and stage-level summary of chemical composition

Text S2. PMF input variables, factor interpretation, and model stability

Text S3. Threshold definition and seasonal sensitivity for high-$PM_{2.5}$ samples

Text S4. ISORROPIA-II thermodynamic diagnostics

Tables S1–S7. Summary of chemical composition, PMF diagnostics, high-PM2.5 threshold sensitivity tests, and thermodynamic diagnostics

Figures S1–S8. Site setting, PMF diagnostics, high-$PM_{2.5}$ sensitivity tests, pH/ALWC diagnostics, PMF factor profiles, and stable-mode solid-salt composition.

Text S1. Detailed chemical analysis, quality control, and stage-level summary of chemical composition

Organic carbon (OC) and elemental carbon (EC) in quartz-fibre filter samples were measured with a Sunset EC/OC analyser (Sunset Laboratory, USA). A 1.5 cm^2 filter punch was placed directly in the quartz boat and analysed using the IMPROVE_A thermal–optical protocol (Chow et al., 2007). The sample was first heated in pure helium to 140, 280, 480, and 580 °C to release OC1, OC2, OC3, and OC4. It was then heated in a He/O2 atmosphere to 580, 740, and 840 °C to release EC1, EC2, and EC3. OC and EC concentrations were calculated after optical correction.

Water-soluble inorganic ions were measured by ion chromatography using a 761 Compact IC (Wang et al., 2006). A 15.904 cm^2 filter piece was ultrasonically extracted twice with a total of 10 mL ultrapure water. The extract was filtered through a 0.22 μm membrane before analysis. The measured species included SO_4^{2-}, NO_3^-, NH_4^+, Na^+, Cl^-, Mg^{2+}, Ca^{2+}, and K^+. The detection limit for water-soluble ions was 10 ng mL^{-1}, and the analytical error was less than 5 %. Before analysis, 1 mL of 200 ppm RbBr was added as an internal standard to correct instrumental response changes.

Trace elements including V, Cr, Mn, Fe, Ni, Cu, Zn, As, Cd, and Pb were measured by inductively coupled plasma mass spectrometry (ICP-MS; ELAN DRC II, PerkinElmer, Hong Kong, China) (Zong et al., 2016; Wang et al., 2006). A separate 61.8 cm^2 filter section was digested with 10 mL of high-purity HNO_3 on a 120 °C hot plate for 120 min. After cooling, the digest was filtered and diluted to 50 mL before analysis. The ICP-MS resolution range was 0.3–3.0 amu, the method detection limit was lower than 0.01 ng mL^{-1}, and the analytical error was less than 5 %. Before analysis, In was added at 5 ppb as an internal standard to correct for instrumental drift and matrix effects.

OC, EC, water-soluble ion, and metal concentrations were corrected using the corresponding mean field blanks before statistical analysis and PMF modelling. Field blanks, laboratory blanks, and replicate samples were used to evaluate background signals introduced during sampling, transport, filter storage, pretreatment, and instrumental analysis, as well as analytical repeatability. Mean blank values for OC and EC were 0.0258 ± 0.0129 and −0.0048 ± 0.0119 μg cm^{-2}, respectively. Blanks for major water-soluble ions were low; mean NO_3^-, SO_4^{2-}, NH_4^+, Na^+, and Ca^{2+} blanks were 0.0352, 0.0225, 0.0311, 0.0185, and 0.0397 mg L^{-1}, respectively. Metal blanks, expressed as concentrations in the ICP-MS digestion solution, were 0.1455, 5.1994, 1.5360, 64.6154, 1.5283, 3.6945, 7.2750, 0.8542, 0.0252, and 0.4896 μg L^{-1} for V, Cr, Mn, Fe, Ni, Cu, Zn, As, Cd, and Pb, respectively.

Stage-level summary of chemical composition

Table S1. Concentrations of $PM_{2.5}$ and measured chemical components in different stages (mean ± standard deviation).

Species	Unit	2012–2013	2017–2020	2021–2023
$PM_{2.5}$	μg m^{-3}	51.75 ± 36.99 (n=119)	47.31 ± 35.52 (n=263)	54.41 ± 44.20 (n=290)
OC	μg m^{-3}	3.83 ± 2.73	2.85 ± 1.95	2.65 ± 2.05

EC	μg m^{-3}	1.46 ± 0.94	1.22 ± 0.90	0.81 ± 0.62
TC (OC+EC)	μg m^{-3}	5.30 ± 3.55	4.06 ± 2.73	3.46 ± 2.53
SO_4^{2-}	μg m^{-3}	9.86 ± 8.33	3.42 ± 3.14	4.10 ± 3.13
NO_3^-	μg m^{-3}	6.31 ± 6.42	4.61 ± 6.05	8.51 ± 11.60
NH_4^+	μg m^{-3}	2.16 ± 1.64	4.16 ± 5.24	3.21 ± 3.30
Cl^-	μg m^{-3}	0.38 ± 0.51	0.31 ± 0.41	0.49 ± 0.51
K^+	μg m^{-3}	0.58 ± 0.58	0.24 ± 0.34	0.27 ± 0.44
Mg^{2+}	μg m^{-3}	0.05 ± 0.04	0.08 ± 0.07	0.11 ± 0.11
Ca^{2+}	μg m^{-3}	0.37 ± 0.48	0.15 ± 0.19	0.51 ± 0.68
Na^+	μg m^{-3}	0.33 ± 0.20	0.50 ± 0.35	0.68 ± 0.49
V	ng m^{-3}	6.19 ± 4.70	1.64 ± 1.44	2.28 ± 2.33
Cr	ng m^{-3}	4.20 ± 4.19	6.19 ± 5.57	7.65 ± 5.96
Mn	ng m^{-3}	220.33 ± 344.08	24.11 ± 23.27	26.24 ± 34.54
Fe	ng m^{-3}	552.93 ± 592.17	466.38 ± 691.51	666.66 ± 1173.27
Ni	ng m^{-3}	4.57 ± 3.67	6.41 ± 6.51	7.09 ± 4.64
Cu	ng m^{-3}	13.09 ± 23.69	16.28 ± 16.68	20.16 ± 14.82
Zn	ng m^{-3}	111.71 ± 164.70	51.27 ± 35.55	45.14 ± 30.43
As	ng m^{-3}	5.10 ± 6.86	4.58 ± 3.13	3.96 ± 5.64
Cd	ng m^{-3}	1.05 ± 1.45	3.94 ± 3.61	2.76 ± 4.77
Pb	ng m^{-3}	102.29 ± 150.10	20.61 ± 13.79	13.51 ± 9.62

Text S2. PMF input variables, factor interpretation, and model stability

The PMF input matrix retained 313 samples with a common set of input species. The input variables included $PM_{2.5}$, OC, EC, eight major water-soluble ions, and ten trace elements. $PM_{2.5}$ and the trace elements were treated as weak variables, whereas the other species were treated as strong variables. Factor interpretation was based on dominant chemical species in the factor profiles, the coastal-port setting of the site, and common source categories used in PMF studies at coastal and regional background sites (Norris et al., 2014; Zong et al., 2018; Wu et al., 2019). The port-emission factor represents an integrated signal related to port activities, ship fuel combustion, coastal aerosol, and regional metal inputs. The combined measurements of major ions, OC/EC, and acid-digested trace elements provide complementary tracers for secondary aerosol, combustion, mineral dust, sea salt, port-related emissions, and industrial-metal sources, thereby supporting the source apportionment conducted here, as in previous PMF applications at regional background and coastal sites (Zong et al., 2016; Liu et al., 2022). Al, Si, Ti, and some refractory components were not measured, and OC represents carbon rather than total organic matter.

Table S2. PMF input species and model variable categories.

Input species	PMF variable category	S/N
$PM_{2.5}$	Weak	1.44
OC	Strong	5.33
EC	Strong	5.53
Na^+	Strong	8.85
NH_4^+	Strong	8.91
K^+	Strong	7.69
Mg^{2+}	Strong	6.41
Ca^{2+}	Strong	8.18
Cl^-	Strong	8.87
NO_3^-	Strong	8.93
SO_4^{2-}	Strong	8.91
V	Weak	5.57
Cr	Weak	5.62
Mn	Weak	5.57
Fe	Weak	5.51
Ni	Weak	5.57
Cu	Weak	5.58
Zn	Weak	5.55
As	Weak	5.57
Cd	Weak	5.59
Pb	Weak	5.58

Factor-number tests covered 4–8 factors. Full Q statistics are summarised in Table S3a and Fig. S2a. As the factor number increased from 4 to 7, Q(Robust) decreased from 26150.6 to 10034.4, Q(True) decreased from 35188.8 to 10917.8, and Q(True)/Q(expected) decreased from 19.61 to 13.79, indicating improved fitting. The 8-factor solution further reduced Q(Robust) to 6431.5, but Q(True)/Q(expected) increased to 14.60 and sea-salt-, metal-, and nitrate-related signals were over-separated. In the 6-factor solution, sea-salt-, port-, and metal-related signals were insufficiently separated. One hundred Base runs were performed, and the unrotated seven-factor Base run 89 was adopted as the main solution.

Species-level fit and scaled-residual diagnostics were evaluated for selected Base run 89 (Table S3c and Fig. S2b). For the major inorganic ions, 93.29 %–100 % of scaled residuals were within −3 to +3; the corresponding proportions were 83.39 % for OC and 84.98 % for EC. Observed–predicted R^2 values were 0.979 for NH_4^+, 0.957 for NO_3^-, 0.846 for SO_4^{2-}, 0.771 for OC, and 0.615 for EC, whereas values were lower for several weak trace-element variables. EC and OC made the largest individual contributions to Q(True), at 15.26 % and 12.81 %, respectively, and no single species dominated total Q(True).

Rotational sensitivity was assessed using different Fpeak values, with Fpeak = 0.5 retained as a sensitivity test rather than as the main solution. Across stage-average and dust-screened high-$PM_{2.5}$ samples, the maximum absolute difference in relative factor contributions between the Base and Fpeak = 0.5 solutions was 0.59 percentage points. Bootstrap mapping rates were 85 %–100 %. DISP returned error code 0 with no factor swaps, and all 147 Fpeak factor–species profile values lay within the corresponding dQ = 4 DISP intervals of the Base solution (Norris et al., 2014; Brown et al., 2015). Some species in the mineral-dust, sea-salt, port-emission, and industrial-metal profiles had wider DISP intervals, so detailed quantitative interpretations of these source factors were treated cautiously (Table S3b and Fig. S3).

Table S3a. Diagnostic results for 4–8-factor PMF solutions.

Number of factors	Q(Robust)	Q(True)	Q(True)/Q(expected)	Interpretation
4	26150.6	35188.8	19.61	Not adopted; secondary ions and mixed sources were insufficiently separated.
5	19014.7	23608.5	16.17	Not adopted; secondary ions and combustion-related signals remained mixed.
6	13844.7	15672.1	13.92	Not adopted; sea-salt, metal, and port-related signals were still insufficiently separated.
7	10034.4	10917.8	13.79	Adopted as the main unrotated Base solution; factor interpretability was satisfactory and Q(True)/Q(expected) was lower than for adjacent solutions.
8	6431.5	6686.1	14.60	Not adopted; Q(Robust) decreased, but source signals were over-separated.

Table S3b. Robustness diagnostics for the selected seven-factor Base solution.

Diagnostic	**Result**	**Interpretation**
Main solution	Seven-factor unrotated Base run 89	Adopted for the main text
Fpeak sensitivity	Fpeak = 0.5; maximum difference of 0.59 percentage points	Stage patterns and late-stage nitrate dominance retained
Bootstrap	Factor mapping rates of 85 %–100 %	Acceptable mapping stability
DISP (dQ = 4)	Error code 0; no swaps; 147/147 Fpeak profile values within the Base intervals	Rotation did not drive the factor profiles

Table S3c. Species-level fit and scaled-residual diagnostics for the selected seven-factor unrotated Base solution. The fraction within −3 to +3 is the percentage of scaled residuals within that interval; the Q contribution is each species' share of Q(True). $PM_{2.5}$ and trace elements were treated as weak variables.

Species	Variable category	Within −3 to +3 (%)	Median scaled residual	Observed–predicted R^2	Q(True) contribution (%)
$PM_{2.5}$	Weak	100.00	0.162	0.423	0.37
OC	Strong	83.39	0.622	0.771	12.81
EC	Strong	84.98	0.653	0.615	15.26
Na^+	Strong	99.04	-0.123	0.946	2.90
NH_4^+	Strong	98.08	0.176	0.979	5.39
K^+	Strong	98.72	-0.054	0.828	2.94
Mg^{2+}	Strong	98.40	-0.121	0.963	2.81
Ca^{2+}	Strong	100.00	-0.002	0.995	0.22
Cl^-	Strong	100.00	0.015	0.992	0.37
NO_3^-	Strong	97.44	-0.061	0.957	3.83
SO_4^{2-}	Strong	93.29	-0.048	0.846	7.16
V	Weak	100.00	0.855	0.216	4.12
Cr	Weak	99.36	1.371	0.240	6.89
Mn	Weak	99.68	0.633	0.056	3.89
Fe	Weak	99.68	0.659	0.299	3.42
Ni	Weak	98.72	0.827	0.248	4.27
Cu	Weak	100.00	1.131	0.064	5.07
Zn	Weak	99.68	0.478	0.178	2.75
As	Weak	98.72	0.921	0.064	4.72
Cd	Weak	99.68	1.348	0.012	6.52
Pb	Weak	99.04	0.714	0.146	4.32

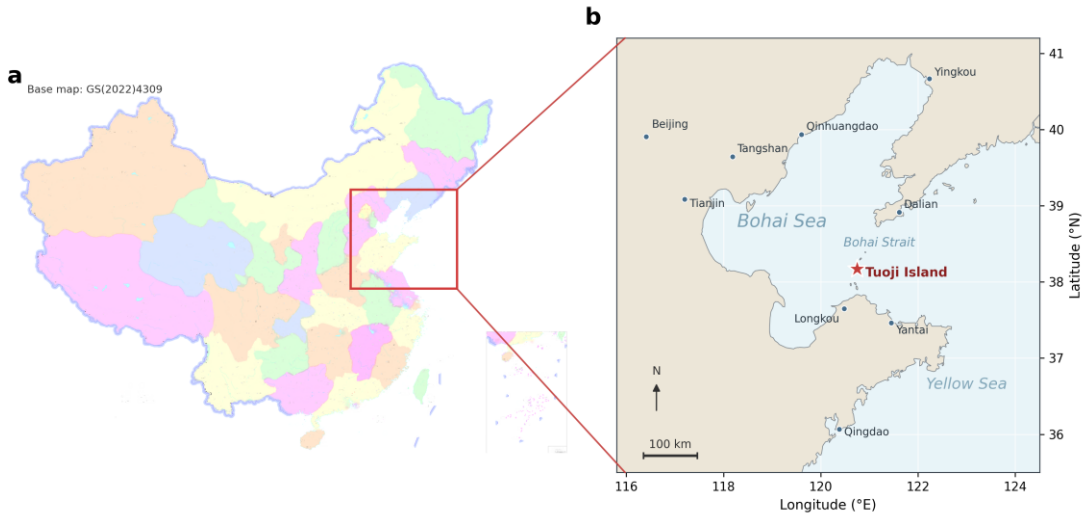

Figure S1. Location of Tuoji Island and selected cities around the Bohai Sea. The China base map was obtained from the Standard Map Service of the Ministry of Natural Resources of China (https://bzdt.ch.mnr.gov.cn/; approval no. GS(2022)4309), and the base-map boundaries were not modified.

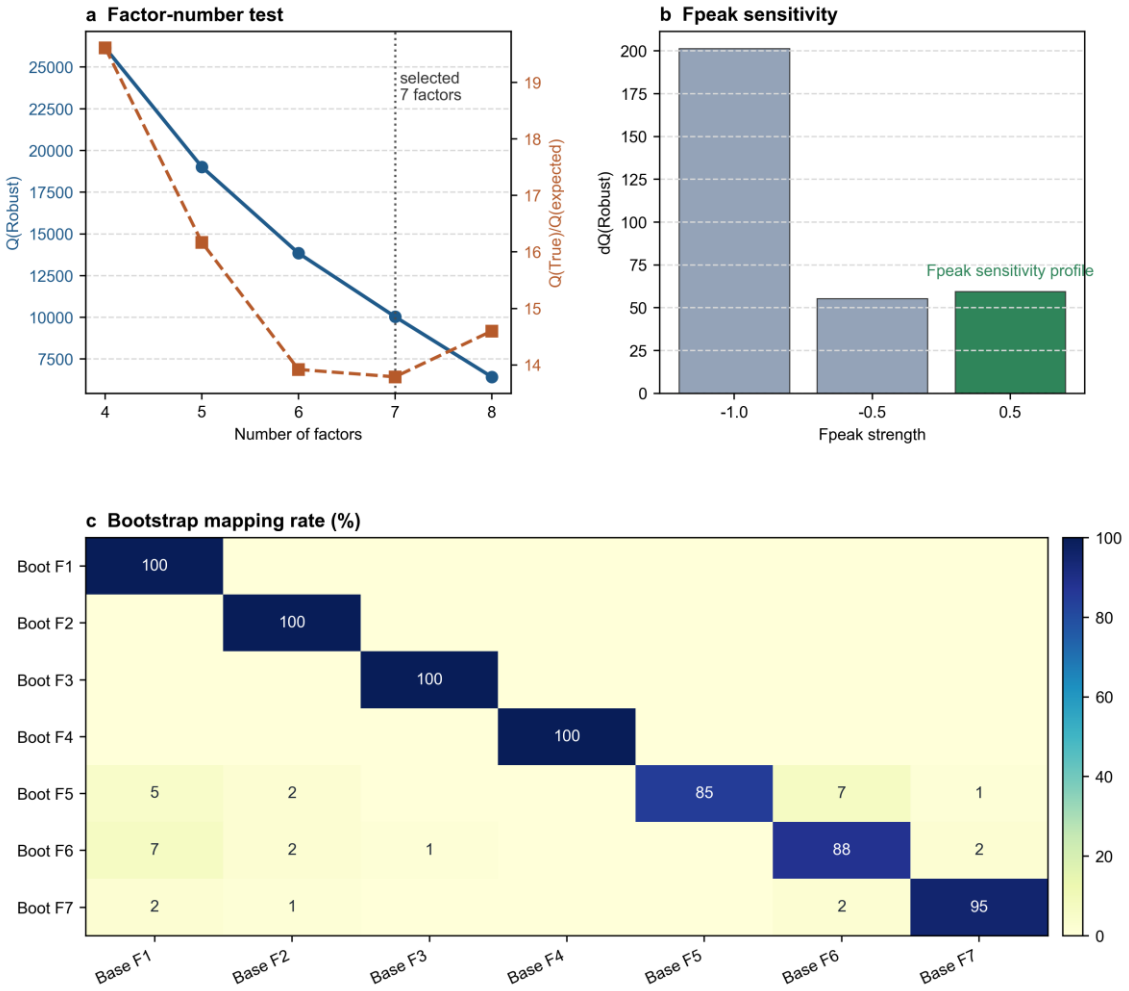

Figure S2a. PMF model diagnostics, including factor-number testing, Fpeak sensitivity, and Bootstrap mapping rates.

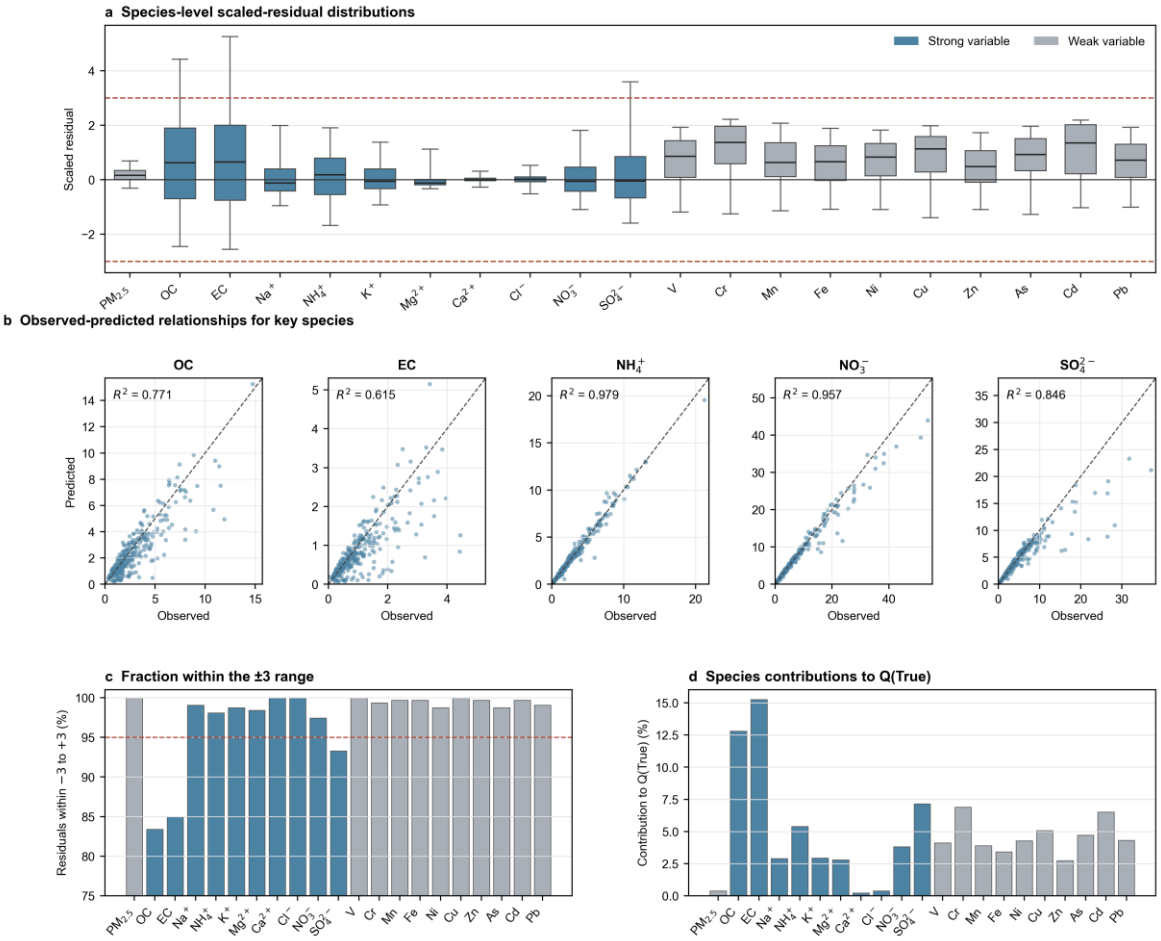

Figure S2b. Species-level fit and scaled-residual diagnostics for the selected seven-factor unrotated Base solution. (a) Scaled-residual distributions; boxes show the interquartile range, centre lines show medians, and whiskers show the 5th–95th percentiles. Dashed lines mark −3 and +3. (b) Observed–predicted relationships for OC, EC, NH_4^+, NO_3^-, and SO_4^{2-}; dashed lines are 1:1 lines. (c) Percentage of scaled residuals within −3 to +3. (d) Species contributions to Q(True). Blue and grey denote strong and weak variables, respectively.

Detailed PMF factor interpretation and chemical profiles

The seven PMF factors used in the main text were interpreted from their chemical profiles, species apportionment percentages, and the coastal-port setting of Tuoji Island. The detailed factor interpretation is provided here to keep the main text focused on stage-dependent changes in source contributions.

F1 is dominated by SO_4^{2-} and NH_4^+, with 66.79 % of SO_4^{2-} and 40.45 % of NH_4^+ assigned to this factor. The $NH_4^+/(2SO_4^{2-})$ molar ratio of 1.04 is close to that expected for ammonium sulfate neutralisation, and the factor is therefore named secondary sulfate (Zong et al., 2018).

F2 is enriched in K^+, OC, and EC, with 85.11 % of K^+, 39.40 % of OC, and 41.50 % of EC assigned to this factor. The OC/EC ratio is 2.83. Previous PMF studies at regional background sites in North China have also used K^+, OC, EC, and OC/EC as important indicators of biomass burning and combustion processes. The co-occurrence of Pb, As, and SO_4^{2-} suggests that F2 is not a pure biomass-burning factor but also includes coal-combustion-related inputs. Samples with the highest 20 % F2 contributions had higher K^+, OC, EC, Pb, and SO_4^{2-} than the remaining samples and occurred mostly in winter–spring and under lower-temperature conditions. Considering northern heating-season coal combustion, biomass burning, and regional transport, F2 is named biomass/coal combustion (Cao et al., 2005; Liu et al., 2022).

F3 is dominated by Ca^{2+}, Fe, and Mg^{2+}, with 93.96 % of Ca^{2+} assigned to this factor. Together with the presence of other crustal elements, this factor is named mineral dust (Zong et al., 2018). F4 is dominated by NO_3^- and NH_4^+, with 77.10 % of NO_3^- and 54.18 % of NH_4^+ assigned to this factor. Its NH_4^+/NO_3^- molar ratio is 1.04, close to the expected NH_4NO_3 stoichiometry, so it is named secondary nitrate. This interpretation is consistent with the increasing contribution of ammonium nitrate in North China (Meng et al., 2022; Zhai et al., 2021). F5 is characterised by Cl^- and Na^+ and is named sea salt (Li et al., 2018; Zhang et al., 2021).

F6 is characterised by Na^+, Fe, Ni, and Cu, with 84.15 % of Na^+, 50.74 % of Cu, 37.99 % of Ni, and 36.30 % of Fe assigned to this factor. Ship-emission profiles generally have high V/Ni ratios, whereas the V/Ni ratio in F6 is only 0.10. This factor is therefore not interpreted as pure ship exhaust. Considering the shipping channels and ports around Tuoji Island, F6 is named the port-emission factor and represents the combined influence of port activities, ship-fuel combustion, coastal aerosols, and regional metal inputs (Liu et al., 2022; Bie et al., 2021; Jang et al., 2023).

F7 is enriched in Cr, Mg^{2+}, Fe, and Ni and is accompanied by Cu, Zn, As, and Cd. A total of 86.13 % of Cr and 83.90 % of Mg^{2+} are assigned to this factor. It is named the industrial-metal factor. Because F7 mainly records metal-input characteristics and contributes little to $PM_{2.5}$ mass, it is not used as a major factor to explain stage-dependent mass changes.

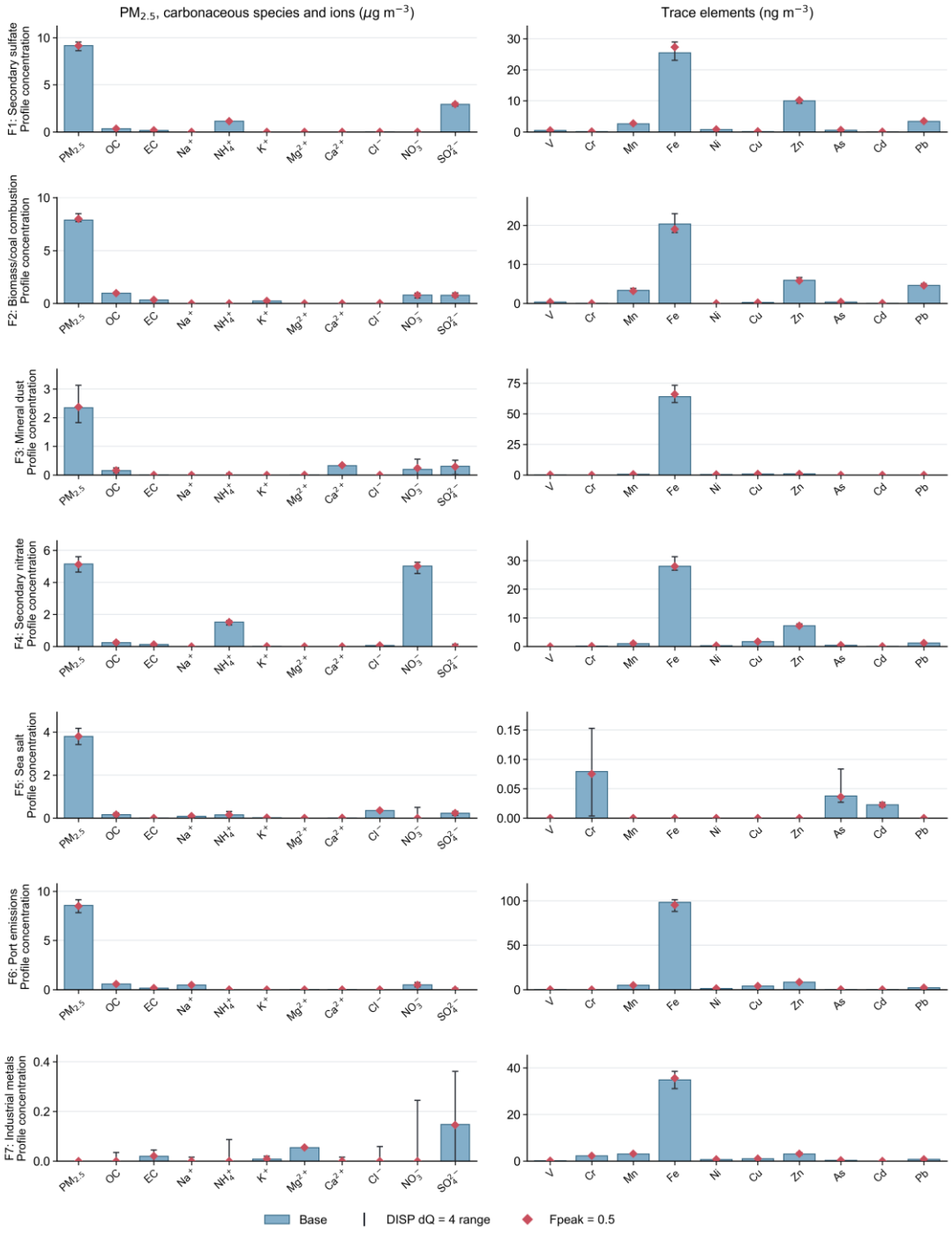

Figure S3. Chemical profiles of the seven-factor Base solution. Bars show Base profile concentrations, error bars show DISP dQ = 4 ranges, and red diamonds show Fpeak = 0.5 profile values. Major species are shown in μg m^{-3} and trace elements in ng m^{-3}.

Text S3. Threshold definition and seasonal sensitivity for high-$PM_{2.5}$ samples

High-$PM_{2.5}$ samples were used to identify which components were relatively amplified under high-$PM_{2.5}$ conditions. Consistent with the main text, mineral-dust outliers were first removed using the concurrent water-soluble Ca^{2+} and elemental Fe anomaly criterion. This criterion follows the high-percentile screening approach of DeBell et al. (2004): water-soluble Ca^{2+} exceeded the site-specific multiyear 95th percentile on every Asian-dust event day, and $PM_{2.5}$ elemental Ca and Fe exceeded at least the 90th percentile and were frequently above the 95th percentile at IMPROVE sites. In this study, samples with both water-soluble Ca^{2+} and elemental Fe above their respective full-sequence 95th percentiles were removed before high-$PM_{2.5}$ selection. To test whether the 20 % threshold was robust, we compared sample size, seasonal-stratification stability, and major component characteristics under three nested thresholds: the highest 10 %, 20 %, and 30 %. Proportion-interval estimates were used to evaluate the uncertainty in seasonal proportion estimates under limited sample sizes. In Tables S4a and S4b, half-widths of the 95 % proportion intervals are given under the conservative case of $p = 0.5$; a larger half-width indicates a less stable seasonal proportion estimate. Minimum expected cell-frequency checks were used to assess whether categorical or stratified comparisons had sufficient counts. This screening procedure removed 2, 0, and 6 mineral-dust outliers in 2012–2013, 2017–2020, and 2021–2023, respectively. The removed dates were 26 April and 27 November 2012; 23 March and 7 May 2021; 26 April 2022; and 9 March, 23 March, and 12 April 2023. After removal, 117, 263, and 284 samples remained for high-$PM_{2.5}$ selection, yielding 24, 53, and 57 high-$PM_{2.5}$ samples using the highest 20 % threshold.

Table S4a. Sample size and statistical stability under different high-$PM_{2.5}$ thresholds.

Stage	Threshold	n	$PM_{2.5}$ threshold (μg m^{-3})	$PM_{2.5}$ median (μg m^{-3})	Samples below 75 μg m^{-3}	Single-sample weight (%)	Wilson half-width (%)	Agresti–Coull half-width (%)	Spring/winter/summer/autumn
2012–2013	Top 10 %	12	110.92	122.91	0	8.3	24.6	24.6	5/3/3/1
2012–2013	Top 20 %	24	84.49	105.53	0	4.2	18.6	18.6	12/6/4/2
2012–2013	Top 30 %	36	61.23	91.90	7	2.8	15.5	15.5	19/7/6/4
2017–2020	Top 10 %	27	84.72	111.12	0	3.7	17.6	17.6	6/18/0/3
2017–2020	Top 20 %	53	63.97	84.72	15	1.9	13.0	13.0	12/30/1/10
2017–2020	Top 30 %	79	53.63	72.61	41	1.3	10.8	10.8	16/40/4/19
2021–2023	Top 10 %	29	112.52	145.56	0	3.4	17.1	17.1	14/8/1/6
2021–2023	Top 20 %	57	72.56	112.52	2	1.8	12.6	12.6	26/15/2/14
2021–2023	Top 30 %	86	57.09	86.95	31	1.2	10.3	10.3	37/27/3/19

Table S4b. Major component characteristics under different high-$PM_{2.5}$ thresholds.

Stage	Threshold	NO_3^- fraction (%)	SO_4^{2-} fraction (%)	NH_4^+ fraction (%)	OC+EC fraction (%)	NO_3^-/SO_4^{2-} ratio
2012–2013	Top 10 %	13.65	16.46	4.15	8.77	0.81
2012–2013	Top 20 %	13.41	17.63	3.79	9.52	0.76
2012–2013	Top 30 %	14.07	17.97	3.81	9.61	0.78
2017–2020	Top 10 %	10.09	6.33	10.95	7.50	1.73
2017–2020	Top 20 %	10.48	5.81	9.71	7.82	1.77
2017–2020	Top 30 %	10.91	6.46	9.23	7.97	1.77
2021–2023	Top 10 %	20.94	5.13	6.23	4.67	4.01
2021–2023	Top 20 %	19.19	5.97	6.00	5.29	3.42
2021–2023	Top 30 %	18.92	6.42	6.20	6.15	3.19

Note: Wilson and Agresti–Coull half-widths were calculated under the conservative case of p = 0.5 and are used to represent the uncertainty in seasonal proportion estimates. Spring/winter/summer/autumn indicates the number of high-$PM_{2.5}$ samples in each season under different thresholds. Under the fixed 75 μg m^{-3} reference, 55 samples during 2021–2023 exceeded this value, and the NO_3^- fraction, SO_4^{2-} fraction, and NO_3^-/SO_4^{2-} ratio were 19.34 %, 5.79 %, and 3.50, respectively, close to the results obtained using the highest 20 % threshold.

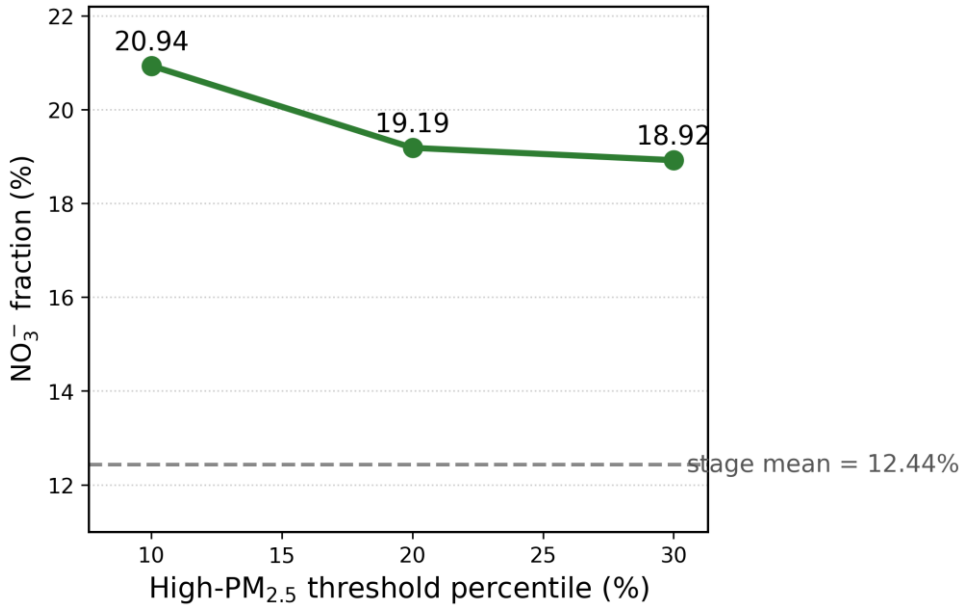

Figure S4. Sensitivity of the NO_3^- fraction in 2021–2023 to the definition of high-$PM_{2.5}$ samples after removal of mineral-dust outliers.

High-$PM_{2.5}$ samples were mainly concentrated in winter and spring, but the seasonal distribution differed among stages. To test whether late-stage nitrate enhancement was solely caused by differences in seasonal distribution, the NO_3^-/SO_4^{2-} ratio in spring and winter high-$PM_{2.5}$ samples was compared after removal of mineral-dust outliers. The NO_3^-/SO_4^{2-} ratio increased from the early to late stages in both spring and winter, indicating that nitrate enhancement cannot be explained solely by differences in seasonal distribution.

Table S5. Seasonal sensitivity of the NO_3^-/SO_4^{2-} ratio in high-$PM_{2.5}$ samples after removal of mineral-dust outliers.

Season	2012–2013	2017–2020	2021–2023
Spring high-$PM_{2.5}$ samples: NO_3^-/SO_4^{2-}	0.93	2.51	3.50
Winter high-$PM_{2.5}$ samples: NO_3^-/SO_4^{2-}	0.48	1.53	3.67

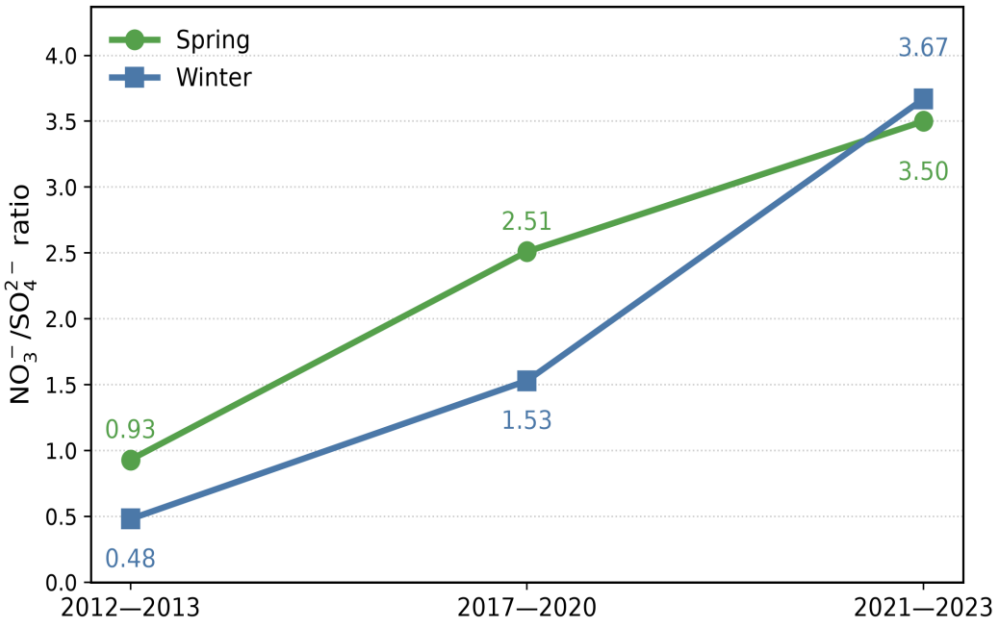

Figure S5. Seasonal sensitivity of the NO_3^-/SO_4^{2-} ratio in high-$PM_{2.5}$ samples after removal of mineral-dust outliers.

Text S4. ISORROPIA-II thermodynamic diagnostics

ISORROPIA-II used particle-phase ions, relative humidity, and temperature as inputs and was run in reverse mode under both stable and metastable assumptions (Fountoukis and Nenes, 2007; Song et al., 2018). Because concurrent gas-phase NH_3, HNO_3, and HCl observations were unavailable, the pH results should not be interpreted as measured aerosol acidity. They are used only as auxiliary diagnostics of relative changes in inorganic aerosol thermodynamic conditions. In the main discussion, ALWC, ion balance, and stage-level changes in the thermodynamic diagnostics are emphasised. Ion-balance and excess-ammonium diagnostics followed previous applications of particle-phase ion stoichiometry (Pathak et al., 2009; Wu et al., 2015). The sample numbers in Table S6 are slightly smaller than the high-$PM_{2.5}$ sample counts in Tables S4a and S4b because only samples with complete ISORROPIA-II input data were used. Stable-mode outputs of model-resolved solid salts are provided in Fig. S8 as a supporting diagnostic for the shift toward NH_4NO_3.

Table S6. Inputs and outputs of ISORROPIA-II metastable thermodynamic diagnostics for high-$PM_{2.5}$ samples with complete thermodynamic input data, defined using the same screening procedure as in the main text. $PM_{2.5}$, ion concentrations, and ALWC are in μg m^{-3}. Ion concentrations, $PM_{2.5}$, RH, ALWC, and pH are medians; temperature is reported as the mean. RH is expressed as a unitless fraction.

Variable	**2012–2013**	**2017–2020**	**2021–2023**
n	22	50	54
$PM_{2.5}$ median (μg m^{-3})	105.53	82.99	110.02
RH median	0.65	0.63	0.68

Variable	2012–2013	2017–2020	2021–2023
T mean (°C)	11.17	6.21	10.17
Na^+ median (μg m^{-3})	0.50	0.69	0.87
SO_4^{2-} median (μg m^{-3})	17.90	4.96	6.05
NH_4^+ median (μg m^{-3})	2.83	6.48	7.02
NO_3^- median (μg m^{-3})	13.78	8.59	21.40
Cl^- median (μg m^{-3})	0.48	0.37	0.69
Ca^{2+} median (μg m^{-3})	0.45	0.07	0.61
K^+ median (μg m^{-3})	1.06	0.08	0.44
Mg^{2+} median (μg m^{-3})	0.08	0.00	0.11
ALWC median (μg m^{-3})	14.95	12.15	22.00
Median diagnostic pH	-0.82	7.39	0.68

Table S7. Sensitivity of reverse-mode pH diagnostic values to ion charge balance for valid samples with complete ion-balance inputs.

Cation/anion equivalent ratio	n	Median pH diagnostic value	Proportion with pH < 4 (%)
<0.8	77	-0.79	100.0
0.8–1.05	152	0.75	69.1
≥1.05	392	7.36	0.5

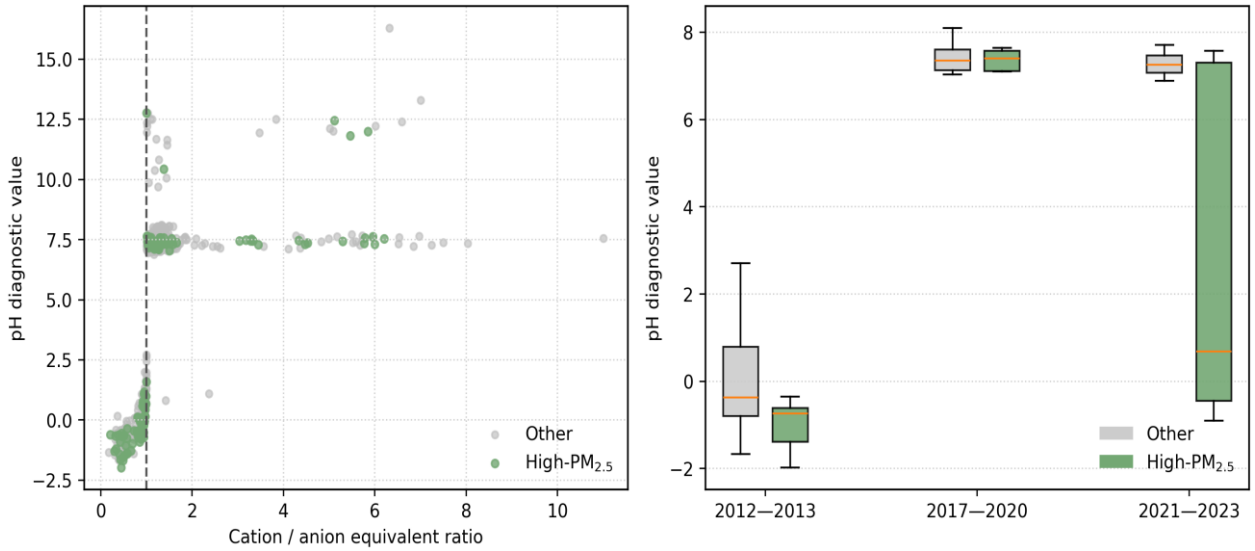

Figure S6. ISORROPIA-II reverse-mode pH diagnostic values and their sensitivity to ion charge balance. The pH values are model diagnostic outputs and do not represent measured aerosol pH.

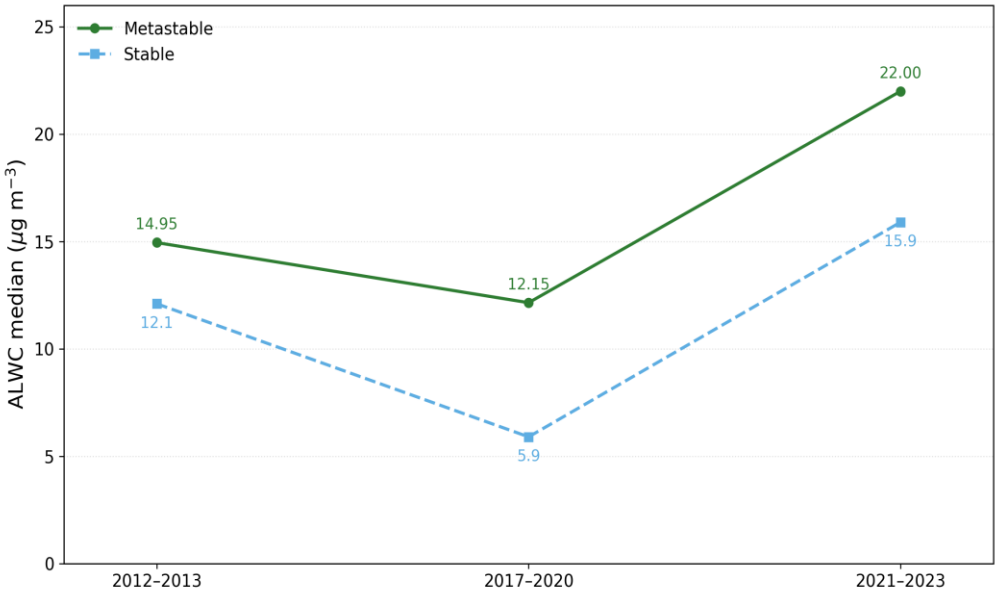

Figure S7. ALWC diagnostic results under stable and metastable assumptions for high-$PM_{2.5}$ samples defined using the same screening procedure as in the main text.

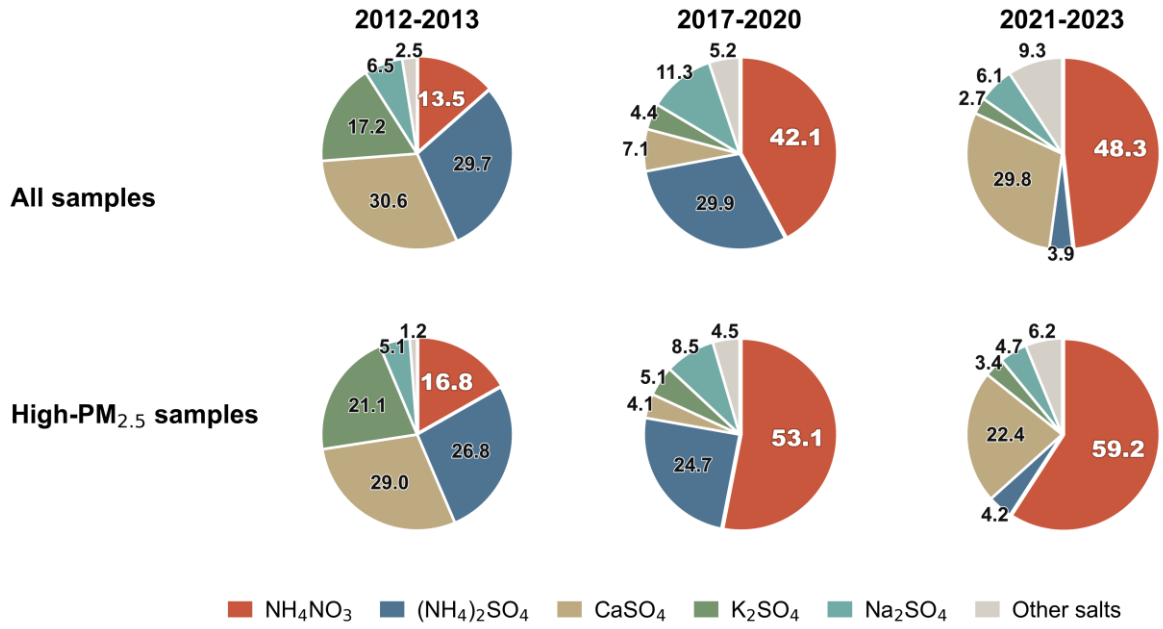

Figure S8. Stage changes in model-resolved solid-salt composition for all samples and high-$PM_{2.5}$ samples under the ISORROPIA-II stable state. Numbers indicate the percentage of each salt in the total model-resolved solid salts. Low-abundance salts are grouped as other salts.

References

Bie, S., Yang, L., Zhang, Y., Huang, Q., Li, J., Zhao, T., Zhang, X., Wang, P., and Wang, W.: Source apportionment of $PM_{2.5}$ in Qingdao Port, East of China, Sci. Total Environ., 755, 142456, https://doi.org/10.1016/j.scitotenv.2020.142456, 2021.

Brown, S. G., Eberly, S., Paatero, P., and Norris, G. A.: Methods for estimating uncertainty in PMF solutions: examples with ambient air and water quality data and guidance on reporting PMF results, Sci. Total Environ., 518–519, 626–635, https://doi.org/10.1016/j.scitotenv.2015.01.022, 2015.

Cao, J. J., Wu, F., Chow, J. C., Lee, S. C., Li, Y., Chen, S. W., An, Z. S., Fung, K. K., Watson, J. G., Zhu, C. S., and Liu, S. X.: Characterization and source apportionment of atmospheric organic and elemental carbon during fall and winter of 2003 in Xi'an, China, Atmos. Chem. Phys., 5, 3127–3137, https://doi.org/10.5194/acp-5-3127-2005, 2005.

Chow, J. C., Watson, J. G., Chen, L. W. A., Chang, M. C. O., Robinson, N. F., Trimble, D., and Kohl, S.: The IMPROVE_A Temperature Protocol for Thermal/Optical Carbon Analysis: Maintaining Consistency with a Long-Term Database, J. Air Waste Manag. Assoc., 57, 1014–1023, https://doi.org/10.3155/1047-3289.57.9.1014, 2007.

DeBell, L. J., Vozzella, M., Talbot, R. W., and Dibb, J. E.: Asian dust storm events of spring 2001 and associated pollutants observed in New England by the Atmospheric Investigation, Regional Modeling, Analysis and Prediction (AIRMAP) monitoring network, J. Geophys. Res., 109, D01304, https://doi.org/10.1029/2003JD003733, 2004.

Fountoukis, C. and Nenes, A.: ISORROPIA II: a computationally efficient thermodynamic equilibrium model for K^+–Ca^{2+}–Mg^{2+}–NH_4^+–Na^+–SO_4^{2-}–NO_3^-–Cl^-–H_2O aerosols, Atmos. Chem. Phys., 7, 4639–4659, https://doi.org/10.5194/acp-7-4639-2007, 2007.

Jang, E., Choi, S., Yoo, E., Hyun, S., and An, J.: Impact of shipping emissions regulation on urban aerosol composition changes revealed by receptor and numerical modelling, npj Clim Atmos Sci, 6, 52, https://doi.org/10.1038/s41612-023-00364-9, 2023.

Li, M., Hu, M., Guo, Q., Tan, T., Du, B., Huang, X., He, L., Guo, S., Wang, W., Fan, Y., and Xu, D.: Seasonal Source Apportionment of $PM_{2.5}$ in Ningbo, a Coastal City in Southeast China, Aerosol Air Qual. Res., 18, 2741–2752, https://doi.org/10.4209/aaqr.2018.01.0011, 2018.

Liu, B., Wang, Y., Meng, H., Dai, Q., Diao, L., Wu, J., Shi, L., Wang, J., Zhang, Y., and Feng, Y.: Dramatic changes in atmospheric pollution source contributions for a coastal megacity in northern China from 2011 to 2020, Atmos. Chem. Phys., 22, 8597–8615, https://doi.org/10.5194/acp-22-8597-2022, 2022.

Meng, F., Zhang, Y., Kang, J., Heal, M. R., Reis, S., Wang, M., Liu, L., Wang, K., Yu, S., Li, P., Wei, J., Hou, Y., Zhang, Y., Liu, X., Cui, Z., Xu, W., and Zhang, F.: Trends in secondary inorganic aerosol pollution in China and its responses to emission controls of precursors in wintertime, Atmos. Chem. Phys., 22, 6291–6308, https://doi.org/10.5194/acp-22-6291-2022, 2022.

Norris, G., Duvall, R., Brown, S., and Bai, S.: EPA Positive Matrix Factorization (PMF) 5.0 Fundamentals and User Guide, U.S. Environmental Protection Agency, EPA/600/R-14/108, 2014.

Pathak, R. K., Wu, W. S., and Wang, T.: Summertime $PM_{2.5}$ ionic species in four major cities of China: nitrate formation in an ammonia-deficient atmosphere, Atmos. Chem. Phys., 9, 1711–1722, https://doi.org/10.5194/acp-9-1711-2009, 2009.

Song, S., Gao, M., Xu, W., Shao, J., Shi, G., Wang, S., Wang, Y., Sun, Y., and McElroy, M. B.: Fine-particle pH for Beijing winter haze as inferred from different thermodynamic equilibrium models, Atmos. Chem. Phys., 18, 7423–7438, https://doi.org/10.5194/acp-18-7423-2018, 2018.

Wang, X., Bi, X., Sheng, G., and Fu, J.: Chemical composition and sources of PM_{10} and $PM_{2.5}$ aerosols in Guangzhou, China, Environ. Monit. Assess., 119, 425–439, https://doi.org/10.1007/s10661-005-9034-3, 2006.

Wu, S. P., Schwab, J., Yang, B. Y., Zheng, A., and Yuan, C. S.: Two-years $PM_{2.5}$ observations at four urban sites along the coast of southeastern China, Aerosol Air Qual. Res., 15, 1799–1812, https://doi.org/10.4209/aaqr.2015.05.0363, 2015.

Wu, S. P., Xu, C., Dai, L. H., Zhang, N., Wei, Y., Gao, Y., Yan, J. P., and Schwab, J. J.: Source apportionment of $PM_{2.5}$ at urban and suburban sites in a port city of southeastern China, Aerosol Air Qual. Res., 19, 2017–2031, https://doi.org/10.4209/aaqr.2019.01.0007, 2019.

Zhai, S., Jacob, D. J., Wang, X., Liu, Z., Wen, T., Shah, V., Li, K., Moch, J. M., Bates, K. H., Song, S., Shen, L., Zhang, Y., Luo, G., Yu, F., Sun, Y., Wang, L., Qi, M., Tao, J., Gui, K., Xu, H., Zhang, Q., Zhao, T., Wang, Y., Lee, H. C., Choi, H., and Liao, H.: Control of particulate nitrate air pollution in China, Nat. Geosci., 14, 389–395, https://doi.org/10.1038/s41561-021-00726-z, 2021.

Zhang, Y., Yang, L., Bie, S., Zhao, T., Huang, Q., Li, J., Wang, P., Wang, Y., and Wang, W.: Chemical compositions and the impact of sea salt in atmospheric PM_1 and $PM_{2.5}$ in the coastal area, Atmos. Res., 250, 105323, https://doi.org/10.1016/j.atmosres.2020.105323, 2021.

Zong, Z., Wang, X., Tian, C., Chen, Y., Qu, L., Ji, L., Zhi, G., Li, J., and Zhang, G.: Source apportionment of $PM_{2.5}$ at a regional background site in North China using PMF linked with radiocarbon analysis: insight into the contribution of biomass burning, Atmos. Chem. Phys., 16, 11249–11265, https://doi.org/10.5194/acp-16-11249-2016, 2016.

Zong, Z., Wang, X., Tian, C., Chen, Y., Fu, S.-F., Qu, L., Ji, L., Li, J., and Zhang, G.: PMF and PSCF based source apportionment of $PM_{2.5}$ at a regional background site in North China, Atmos. Res., 203, 207–215, https://doi.org/10.1016/j.atmosres.2017.12.013, 2018.